Atmospheric
Chemistry
and Physics

Supplement of

New particle formation induced by anthropogenic–biogenic interactions on the southeastern Tibetan Plateau

Shiyi Lai et al.

Correspondence to: Ximeng Qi (qiximeng@nju.edu.cn) and Xin Huang (xinhuang@nju.edu.cn)

Section S1. Description of in situ instrumentation

The particle number size distributions (PNSDs) in the size range from 1 nm to 20 μm were collectively measured using five instruments, including a Particle Size Magnifier (PSM, Airmodus Inc.), a Neutral cluster and Air Ion Spectrometer (NAIS, Ariel Inc.), two Scanning Mobility Particle Sizers (nano-SMPS and long-SMPS, TSI Inc.) and an Aerodynamic Particle Sizer (APS, TSI Inc.). The PSM was operated in the scanning mode, with the saturator flow rate continuously changing from 0.1 L min^{-1} to 1.3 L min^{-1}. The NAIS observed air ion number size distributions from 0.8 nm to 40 nm and particle number size distributions from 2 nm to 40 nm. The nano-SMPS and long-SMPS share similar configurations but differ by a differential mobility analyzer (DMA) and a condensation particle counter (CPC) for measuring PNSDs in the size range of 4–70 nm and 12–540 nm, respectively. The APS measures the PNSD from 500 nm to 20 μm in the aerodynamic diameter. The sample air of nano-SMPS, long-SMPS and APS were dried using the silica gel dryer. The inlet flow rate of PSM, NAIS, nano-SMPS, long-SMPS and APS were 2.5 L min^{-1}, 54 L min^{-1}, 1.5 L min^{-1}, 1 L min^{-1} and 5 L min^{-1}, respectively. Throughout the intensive campaign, nano-SMPS and long-SMPS shared one inlet tube while the other instruments used separated inlet tubes. The PNSD in the overlapping size ranges detected by different particle sizers demonstrated good agreement. To obtain the PNSD from 4 nm to 1000 nm, the SMPS data and APS data were merged by following the method described by Beddows et al. (2010). The time resolution of PSM, NAIS, nano-SMPS, long-SMPS and APS data were 4 min, 3.5 min, 5.5 min, 5.5 min and 5.5 min, respectively.

The monoterpene concentration was measured by a Proton Transfer Reaction Time-Of-Flight Mass Spectrometer (PTR-TOF-MS, Ionicon Analytik Inc.). During the campaign, the transmission function of the PTR-TOF-MS was calibrated with a 15-component gas mixture standard that included isoprene, α-pinene, benzene, and toluene.

A nitrate Chemical Ionization with the Atmospheric Pressure interface Time-Of-Flight mass spectrometer (CI-APi-TOF, Aerodyne Research Inc.) was used to detect the H$_2$SO$_4$ and HOMs (Jokinen et al., 2012). The sample air was drawn into CI-APi-TOF through a stainless-steel tube (100 cm long, 3/4 inch diameter) with a flow rate of 10 L min^{-1}. The sample flow was then surrounded by a clean sheath flow (25 L min^{-1}) containing nitrate reagent ions in a laminar flow reactor. The nitrate reagent ions in the sheath flow were generated by exposing air containing nitric acid to a photoionizer X-ray (Model L9491, Hamamatsu Inc.). H$_2$SO$_4$ was calibrated during the campaign by utilizing a stable and adjustable concentration H$_2$SO$_4$ source (Kürten et al., 2012). The mass-dependent transmission correction of the CI-APi-TOF was determined by following the method described by Heinritzi et al. (2016), by depleting the reagent ions with several perfluorinated acids before the campaign. To detect the natural cluster ions, the CI-APi-TOF mode was switched to APi-TOF mode by switching off the sheath flow and photoionizer X-ray and setting the ion voltage and drift voltage in laminar flow reactor to zero. On a typical NPF (29 Apirl 2021) day, the mass spectrometer was alternated between CI-APi-TOF mode and APi-TOF mode at a frequency of once per hour from 10:00 to 21:00 (UTC+8), with each mode running 1 hour.

Section S2. Description of the modified VBS framework

Previous studies have demonstrated that oxidation of monoterpene could generate large amounts of ultra- and extremely low-volatility organic compounds, which are important precursors for NPF (Ehn et al., 2014). Thus, in our study, the peroxy radicals (RO_2) chemistry we accounted for is specific to monoterpenes. The modified volatility basis set (VBS) framework we used in WRF-Chem explicitly represents peroxy radicals (RO_2) chemistry and distributes products into the appropriate volatility bins after RO_2 termination into stable molecules. In the modified VBS framework, organic species are lumped into the C* bins, with C* ranging from 10^{-9} to 10^5 µg m^{-3}, separated by powers of 10^2 (i.e., 8 bins in total).

The reactions begin with oxidation of monoterpene with O_3, OH, and NO_3, producing peroxy radicals (RO_2). The model distinguishes two types of peroxy radicals: one with the potential for autoxidation and the other without. The radical termination proceeds via unimolecular termination or reactions with HO_2, NO, or another peroxy radical. Peroxy radical cross-reactions can produce dimers (ROOR), and the fraction of dimers in all cross-reaction products is assumed to depend on the volatility of the reacting peroxy radicals. The non-dimer cross-reaction products, as well as the termination products via unimolecular termination or reaction with NO, undergo either functionalization or fragmentation. The reactions and rate coefficients in our work are summarized in Table S1 of Schervish and Donahue (2020). It is noteworthy that the mechanism of peroxy radical autoxidation used in this study was similar with that in PRAM/autoPRAM (Roldin et al., 2019), but it is a simplified version due to the computational efficiency of the regional transport model. We map the stable molecules generated from each peroxy radical termination pathway to a distribution of species in the VBS space through kernels, allowing us to represent the wide variety of both peroxy radicals and stabilization reactions (Schervish and Donahue, 2020). The kernels used in this work are summarized in Tables S3–S6 of Schervish and Donahue (2020).

It should be noted that we improved the WRF-Chem model based on the mechanism of alpha-pinene oxidation, as a large number of lab experiments have thoroughly investigated this mechanism. However, various monoterpenes including alpha-pinene, beta-pinene and limonene are grouped together in the WRF-Chem, which leads to the uncertainties in the modelling of HOMs. The yield of HOMs is higher for alpha-pinene than for beta-pinene, while lower than for limonene (Ehn et al., 2014).

Section S3. The temperature dependence for organic nucleation

The temperature dependence function for organic nucleation in our study is derived from the work of Dunne et al. (2016). Dunne et al. (2016) determined the temperature dependence through the Atmospheric Cluster Dynamics Code model (ACDC) studies based on quantum chemical calculations of cluster binding energies. They used the organic proxy compound 3-methyl-1,2,3-butane-tricarboxylic acid (MBTCA) for their calculations. MBTCA was chosen because it is a well-known compound formed in the oxidation of volatile organic compounds and has a high O:C ratio. The formation free energies for MBTCA-sulfuric acid clusters were already available from previous works (Riccobono et al., 2014).

However, it's important to note that this estimation could potentially lead to a stronger temperature dependence than reality. This is because the isomerization reactions that create organic molecules with sufficiently low volatility to participate in nucleation are slower at low temperatures. In these cases, instead of isomerization, organic peroxy radicals react with other peroxy radicals to create stable, less oxidized species, leading to a decrease in oxidation levels. To address this, Dunne et al. (2016) proposed a plausible weaker temperature dependence, which lies between the extremes of zero temperature dependence and the MBTCA case. The expression used for the temperature dependence is as follows:

Jorg' = Jorg exp(−(T − 278)/10)

This formula represents the temperature dependence we apply in our model.

Section S4. The contribution of NPF to CCN

To estimate the number of Cloud Condensation Nuclei (CCN), we used a tracer-based method as described in Kulmala et al. (2016). Black carbon (BC) was used as the indicator for primary aerosol particles. Here, we used the number concentration of particles larger than 50 nm (referred to as $NC_{>50\,nm}$) as a proxy for CCN. The number concentration of primary CCN was obtained using the following equation:

$$NC_{>50nm,\ primary} = S1 \times [BC]$$

where [BC] represents the BC mass concentration, and S1 is a semi-empirical scaling factor. The S1 was determined from the relationship between the simultaneous measurements of $NC_{>50\,nm}$ and [BC]. Specifically, 0.5% of the data points in the $NC_{>50\,nm}$ vs. [BC] scatter plot fell below the line S1×[BC]. Finally, we obtained the number concentration of secondary CCN using the following formula:

$$NC_{>50nm,secondary} = NC_{>50nm,total} - NC_{>50nm,primary}$$
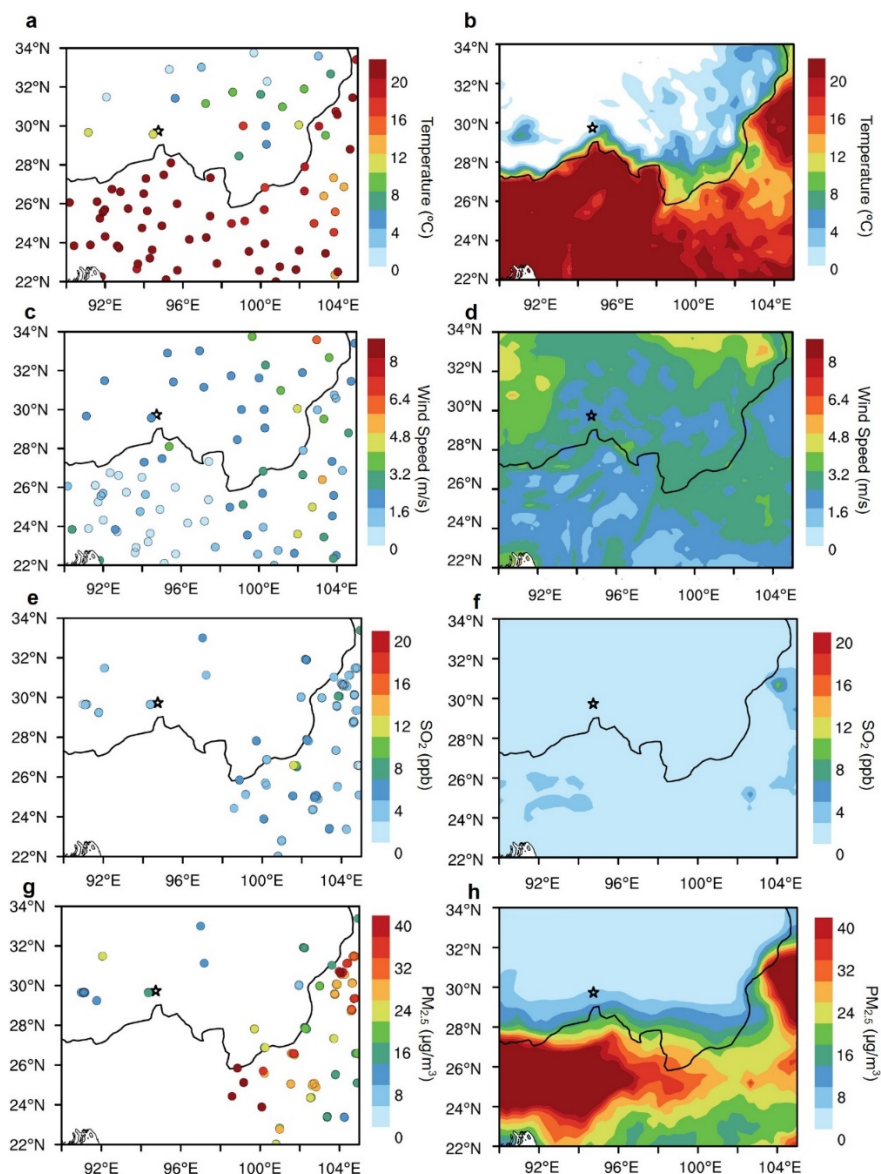
Figure S1. Averaged spatial distributions of (a) observed and (b) simulated 2-m temperature; (c) observed and (d) simulated 10-wind speed temperature; (e) observed SO_2 at Chinese national air quality monitoring stations and (f) simulated SO_2 concentrations; and (g) observed $PM_{2.5}$ concentrations at Chinese national air quality monitoring stations and (h) simulated $PM_{2.5}$ concentrations during 28–30 April. Here, the surface weather data are accessible at the Integrated Surface Database (https://www.ncei.noaa.gov/products/land-based-station/integrated-surface-database). The air quality dataset at the national monitoring stations is obtained from the China National Environmental Monitoring Centre.
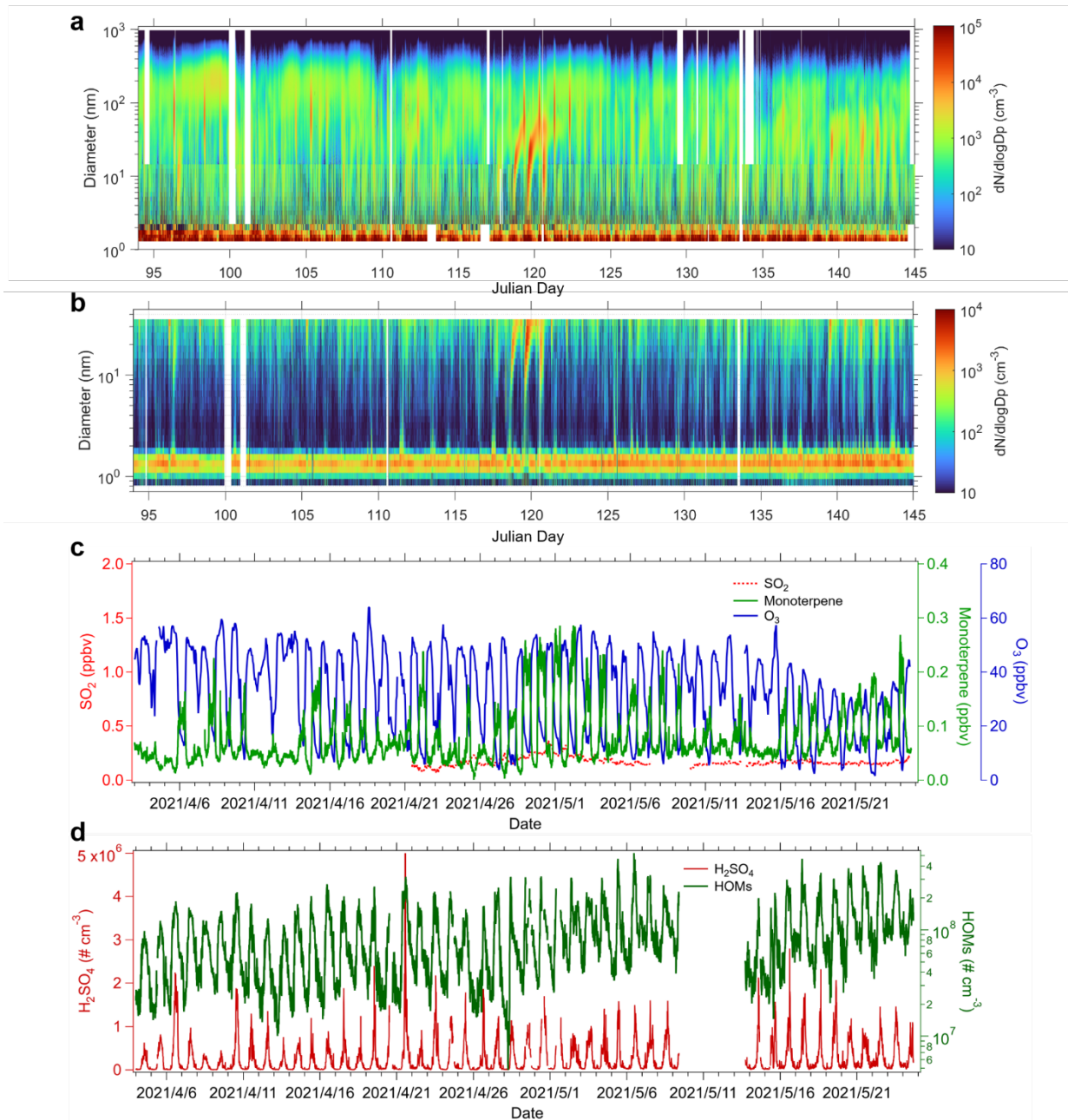
Figure S2. Time series of (a) particle number size distribution from 1 nm to 1000 nm, (b) positive ion number size distribution from 0.8 nm to 40 nm, (c) SO_2, monoterpene and O_3 concentrations, and (d) sulfuric acid and HOMs concentrations in Lulang during the observation campaign from 4 April to 24 May, 2021.
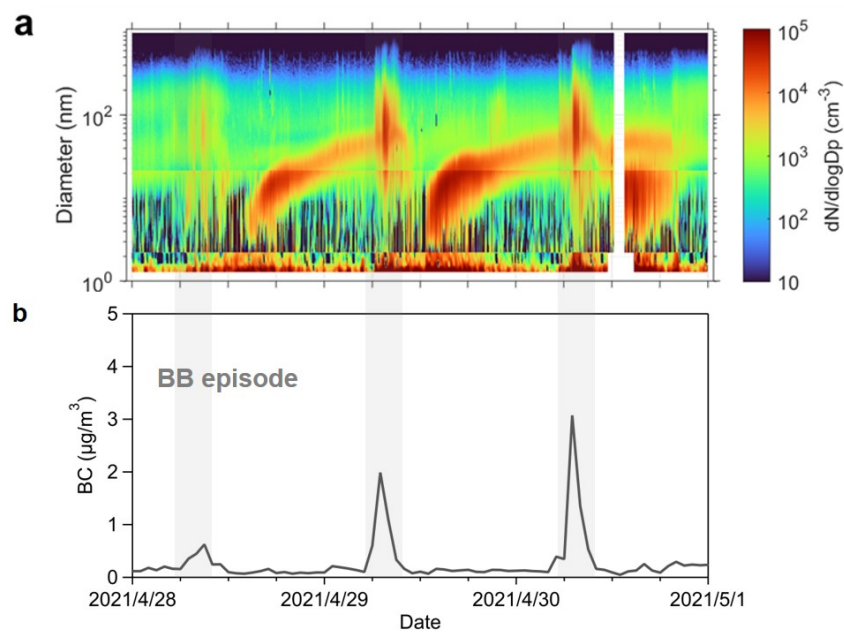
Figure S3. (a) Temporal evolutions of particle number size distribution and (b) BC concentrations measured in Lulang during 28–30 April, 2021. All time is in the UTC+8 time zone in this study.
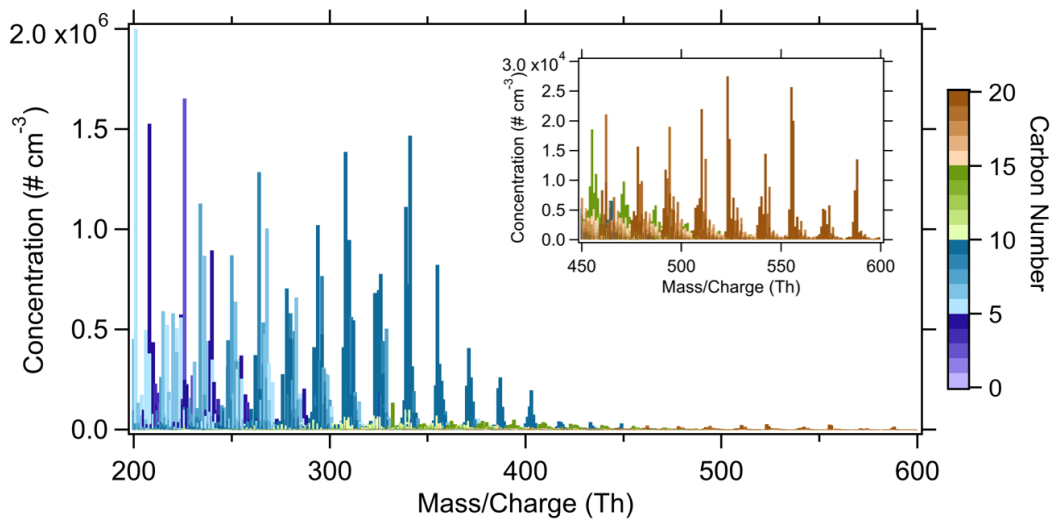
Figure S4. Mass spectrum of neutral clusters, colored by carbon number, observed by CI-APi-TOF from 28 April to 30 April 2020. Note that the top right subplot is zoomed-in view of m/z 450-600.
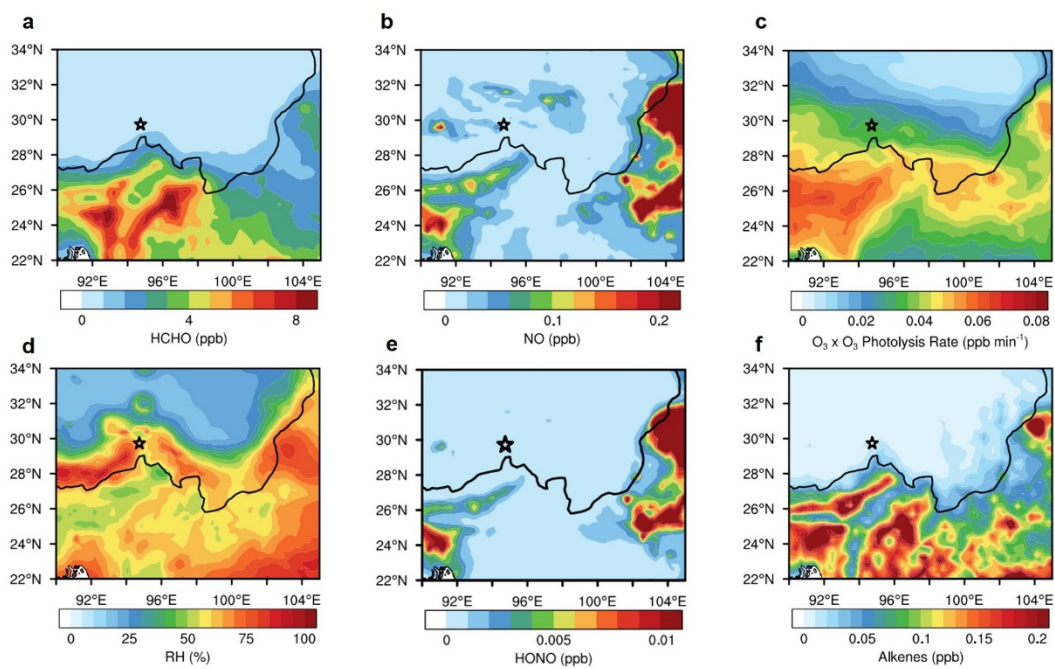
Figure S5. Average spatial distributions of simulated near-surface (a) formaldehyde (HCHO) concentrations, (b) NO concentrations, (c) $O_3 \times O_3$ photolysis rate, (d) relative humidity, (e) nitrous acid (HONO) concentrations, (f) alkenes concentrations during 28–30 April. Note: The black star marks the location of the Lulang site.
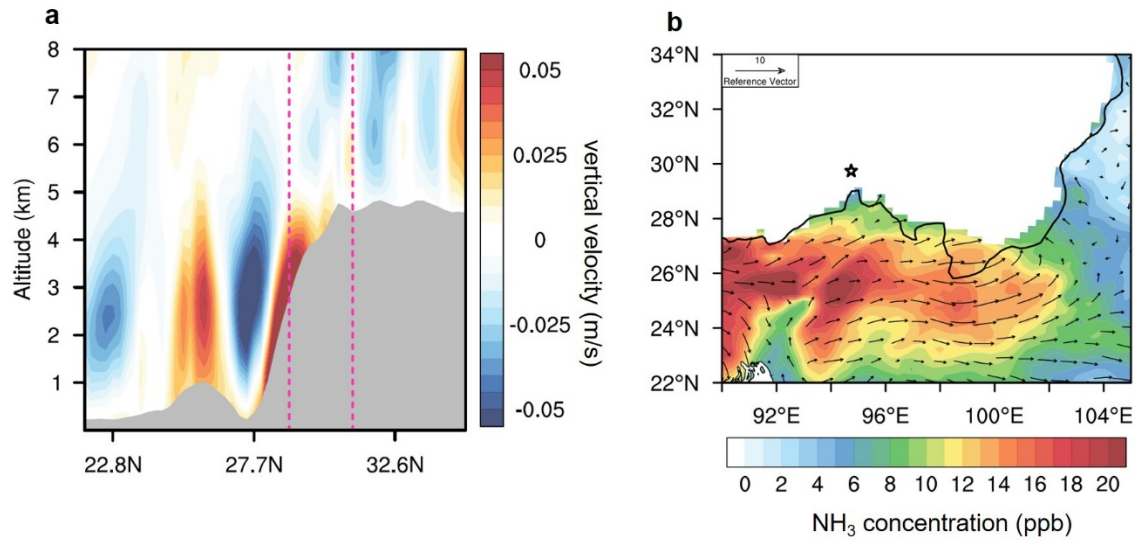
Figure S6. (a) Latitude–height cross sections of vertical velocity averaged along 94–96°E from 12:00 to 18:00 (UTC+8) during 28–30 April. Note: The pink dashed lines show the location of the research domain marked in Fig.6a. (b) Spatial distributions of simulated NH₃ concentration together with wind fields at 3000 m averaged from 12:00 to 18:00 (UTC+8) during 28–30 April.
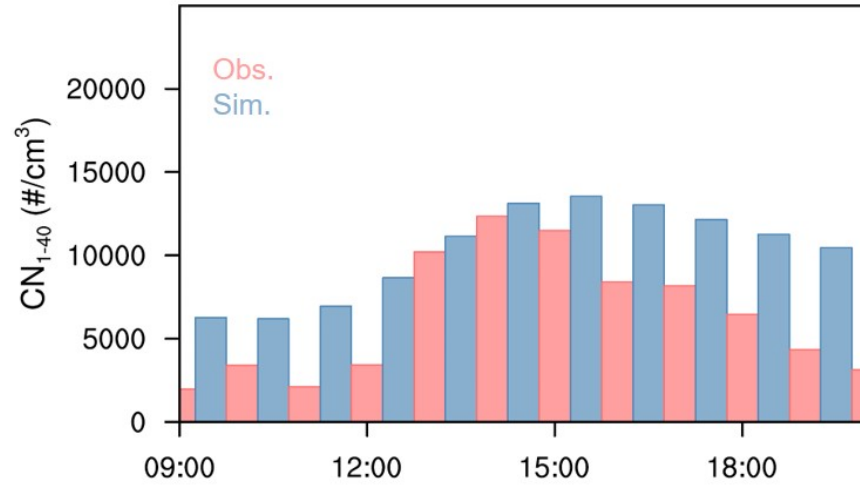
Figure S7. Diurnal evolutions of observed and simulated 1-40 nm particle number concentrations averaged during 28–30 April over the research domain.
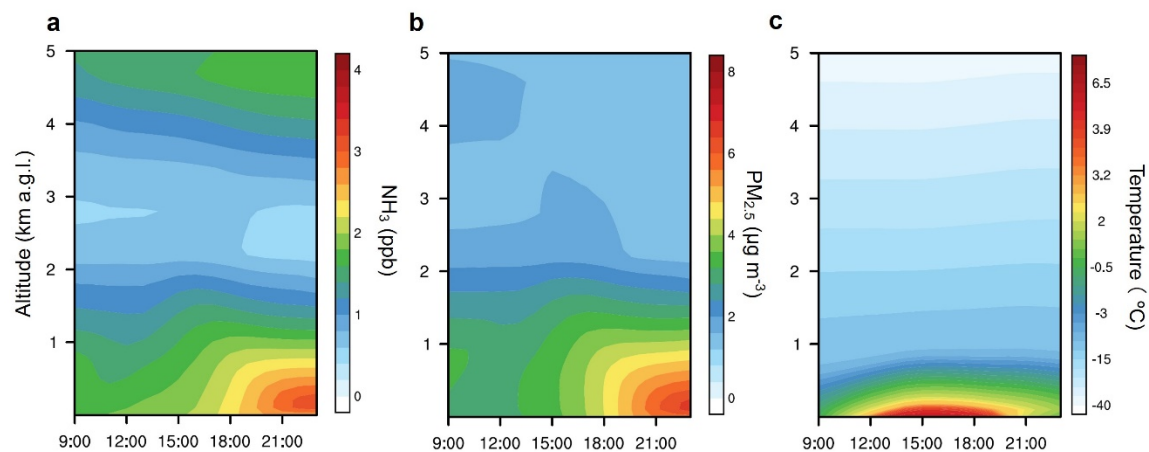
Figure S8. (a) Averaged diurnal evolution of vertical cross section of simulated NH_3 concentrations over region indicated by pink dashed rectangle in Fig. 6a during 28–30 April. (b) Same as Fig. S1a but for $PM_{2.5}$ concentrations. (c) Same as Fig. S1a but for air temperature.

Table S1. The statistics of NPF parameters in Lulang. Note: the NPF start and end time, formation rate ($J_{1.5\ nm}$ and $J_{3\ nm}$) and growth rate ($GR_{<3\ nm}$, $GR_{3-7\ nm}$, $GR_{7-15\ nm}$) are the median values.

Parameter	Value
NPF frequency	21.3%
NPF frequency of clear-sky day	66.7%
NPF start time (UTC+8)	11:50
NPF end time (UTC+8)	17:00
$J_{1.5\ nm}$ ($cm^{-3}\ s^{-1}$)	1.3
$J_{3\ nm}$ ($cm^{-3}\ s^{-1}$)	0.2
$GR_{<3\ nm}$ ($nm\ h^{-1}$)	0.6
$GR_{3-7\ nm}$ ($nm\ h^{-1}$)	2.5
$GR_{7-15\ nm}$ ($nm\ h^{-1}$)	5.4

References

Beddows, D. C. S.,Dall'osto, M. , and Harrison, R. M.: An Enhanced Procedure for the Merging of Atmospheric Particle Size Distribution Data Measured Using Electrical Mobility and Time-of-Flight Analysers, Aerosol Sci. Technol., 44, 930-938, 10.1080/02786826.2010.502159, 2010.

Dunne, E. M.,Gordon, H.,Kurten, A.,Almeida, J.,Duplissy, J.,Williamson, C.,Ortega, I. K.,Pringle, K. J.,Adamov, A.,Baltensperger, U.,Barmet, P.,Benduhn, F.,Bianchi, F.,Breitenlechner, M.,Clarke, A.,Curtius, J.,Dommen, J.,Donahue, N. M.,Ehrhart, S.,Flagan, R. C.,Franchin, A.,Guida, R.,Hakala, J.,Hansel, A.,Heinritzi, M.,Jokinen, T.,Kangasluoma, J.,Kirkby, J.,Kulmala, M.,Kupc, A.,Lawler, M. J.,Lehtipalo, K.,Makhmutov, V.,Mann, G.,Mathot, S.,Merikanto, J.,Miettinen, P.,Nenes, A.,Onnela, A.,Rap, A.,Reddington, C. L.,Riccobono, F.,Richards, N. A.,Rissanen, M. P.,Rondo, L.,Sarnela, N.,Schobesberger, S.,Sengupta, K.,Simon, M.,Sipila, M.,Smith, J. N.,Stozkhov, Y.,Tome, A.,Trostl, J.,Wagner, P. E.,Wimmer, D.,Winkler, P. M.,Worsnop, D. R. , and Carslaw, K. S.: Global atmospheric particle formation from CERN CLOUD measurements, Science, 354, 1119-1124, 10.1126/science.aaf2649, 2016.

Ehn, M.,Thornton, J. A.,Kleist, E.,Sipila, M.,Junninen, H.,Pullinen, I.,Springer, M.,Rubach, F.,Tillmann, R.,Lee, B.,Lopez-Hilfiker, F.,Andres, S.,Acir, I. H.,Rissanen, M.,Jokinen, T.,Schobesberger, S.,Kangasluoma, J.,Kontkanen, J.,Nieminen, T.,Kurten, T.,Nielsen, L. B.,Jorgensen, S.,Kjaergaard, H. G.,Canagaratna, M.,Maso, M. D.,Berndt, T.,Petaja, T.,Wahner, A.,Kerminen, V. M.,Kulmala, M.,Worsnop, D. R.,Wildt, J. , and Mentel, T. F.: A large source of low-volatility secondary organic aerosol, Nature, 506, 476-479, 10.1038/nature13032, 2014.

Heinritzi, M.,Simon, M.,Steiner, G.,Wagner, A. C.,Kürten, A.,Hansel, A. , and Curtius, J.: Characterization of the mass-dependent transmission efficiency of a CIMS, Atmospheric Measurement Techniques, 9, 1449-1460, 10.5194/amt-9-1449-2016, 2016.

Jokinen, T.,Sipila, M.,Junninen, H.,Ehn, M.,Lonn, G.,Hakala, J.,Petaja, T.,Mauldin, R. L.,Kulmala, M. , and Worsnop, D. R.: Atmospheric sulphuric acid and neutral cluster measurements using CI-APi-TOF, Atmos. Chem. Phys., 12, 4117-4125, 10.5194/acp-12-4117-2012, 2012.

Kulmala, M.,Luoma, K.,Virkkula, A.,Petaja, T.,Paasonen, P.,Kerminen, V. M.,Nie, W.,Qi, X. M.,Shen, Y. C.,Chi, X. G. , and Ding, A. J.: On the mode-segregated aerosol particle number concentration load: contributions of primary and secondary particles in Hyytiala and Nanjing, Boreal Environ. Res., 21, 319-331, 2016.

Kürten, A.,Rondo, L.,Ehrhart, S. , and Curtius, J.: Calibration of a Chemical Ionization Mass Spectrometer for the Measurement of Gaseous Sulfuric Acid, Journal of Physical Chemistry A, 116, 6375-6386, 10.1021/jp212123n, 2012.

Riccobono, F.,Schobesberger, S.,Scott, C. E.,Dommen, J.,Ortega, I. K.,Rondo, L.,Almeida, J.,Amorim, A.,Bianchi, F.,Breitenlechner, M.,David, A.,Downard, A.,Dunne, E. M.,Duplissy, J.,Ehrhart, S.,Flagan, R. C.,Franchin, A.,Hansel, A.,Junninen, H.,Kajos, M.,Keskinen, H.,Kupc, A.,Kurten, A.,Kvashin, A. N.,Laaksonen, A.,Lehtipalo, K.,Makhmutov, V.,Mathot, S.,Nieminen, T.,Onnela, A.,Petaja, T.,Praplan, A. P.,Santos, F. D.,Schallhart, S.,Seinfeld, J. H.,Sipila, M.,Spracklen, D. V.,Stozhkov, Y.,Stratmann,

F.,Tome, A.,Tsagkogeorgas, G.,Vaattovaara, P.,Viisanen, Y.,Vrtala, A.,Wagner, P. E.,Weingartner, E.,Wex, H.,Wimmer, D.,Carslaw, K. S.,Curtius, J.,Donahue, N. M.,Kirkby, J.,Kulmala, M.,Worsnop, D. R. , and Baltensperger, U.: Oxidation products of biogenic emissions contribute to nucleation of atmospheric particles, Science, 344, 717-721, 10.1126/science.1243527, 2014.

Roldin, P.,Ehn, M.,Kurten, T.,Olenius, T.,Rissanen, M. P.,Sarnela, N.,Elm, J.,Rantala, P.,Hao, L. Q.,Hyttinen, N.,Heikkinen, L.,Worsnop, D. R.,Pichelstorfer, L.,Xavier, C.,Clusius, P.,Ostrom, E.,Petaja, T.,Kulmala, M.,Vehkamaki, H.,Virtanen, A.,Riipinen, I. , and Boy, M.: The role of highly oxygenated organic molecules in the Boreal aerosol-cloud-climate system, Nat. Commun., 10, 15, 10.1038/s41467-019-12338-8, 2019.

Schervish, M. , and Donahue, N. M.: Peroxy radical chemistry and the volatility basis set, Atmos. Chem. Phys., 20, 1183-1199, 10.5194/acp-20-1183-2020, 2020.